

Research paper

3D printed wood-fiber reinforced architected cellular composite beams with engineered flexural properties



Ehsan Estakhrianhaghghi^a, Armin Mirabolghasemi^a, Larry Lessard^b,
Abdolhamid Akbarzadeh^{a,b,*}

^a Department of Bioresource Engineering, McGill University, Island of Montreal, QC H9X 3V9, Canada

^b Department of Mechanical Engineering, McGill University, Montreal, QC H3A 0C3, Canada

ARTICLE INFO

Keywords:
Architected cellular structures
Sustainable materials
Wood-fiber reinforced composites
Engineered mechanical properties

ABSTRACT

This study explores the integration of cellulose-based compounds into a biobased polymer to create high-performance sustainable materials with improved properties. The elastic flexural characteristics of 3D printed composites, comprised of polylactic-acid (PLA) biopolymer reinforced by a variety of waste wood fiber weight percentage (2.5%–15%), are investigated. Initial steps involve producing wood-fiber reinforced PLA (WF-PLA) filaments and the 3D printing of test specimens. Experimental outcomes reveal enhanced flexural modulus (60% increase), rigidity (72% increase), strength (39% increase), and failure strain (21% increase) alongside reduced composite coupon density (5.2% decrease), attributed to wood fiber incorporation. To achieve lightweight and sustainable structural components with tunable attributes, architected composite cellular beams are introduced. These beams comprised of wood-fiber reinforced composites feature cross-sectional unit cells with one or two reflection symmetries, showcasing the synergy between architecture and material composition in enhancing quasi-isotropic flexural rigidity. Investigation on the flexural rigidity ratio ($[EI]_{yy}/[EI]_{xx}$) involves theoretical modeling, computational analysis, and experimental validation using 3D printed samples. WF-PLA filaments enable the 3D printing of engineered quasi-isotropic cellular beams, termed “Isoflex”, that demonstrate up to 130% enhanced specific flexural rigidity (bending rigidity-to-mass ratio) and up to 70% improvement in flexural rigidity ratio to have isotropic flexural properties, compared to pure PLA beams. This study introduces WF-PLA engineered cellular composites as a sustainable avenue for tuning structural properties, contributing to the realm of additive manufacturing.

1. Introduction

Lightweight architected cellular solids with rationally-designed microarchitecture and material composition offer a low-mass solution for achieving high stiffness/strength-to-weight ratios and tunable multiphysical properties [1,2]. *Cellular solids*, also known as cellular metamaterials when delivering unprecedented properties beyond what conventional materials offer, have lately been identified for their prospective applications in the automotive, aerospace, robotics, energy and biomedical sectors, offering attributes such as high energy absorption/dissipation capacity and programmable shape-changing, vibration, and acoustic properties [3–8]. The growing demand for multifunctional and recyclable composite polymers, coupled with the advancements in additive manufacturing, has spurred research into cost-effective and sustainable materials with enhanced functionalities. 3D printing or

additive manufacturing technology uses a predefined Computer Aided Design (CAD) model to fabricate free-form materials and structures. The key advantages of 3D printing include fast prototyping, material savings, material waste minimization, design flexibility and the ability to fabricate complicated architectures [9,10]. Among various investigations on materials used in 3D printing, biobased Polylactic Acid (PLA) has gained prominence due to its cost-effectiveness, ease of manufacturing, and biodegradability [11–13]. Advances in 3D printing technologies have imparted potentials for reinforcing PLA with fibers to 3D print fiber-reinforced composites with improved mechanical and thermal properties [14]. Furthermore, there has been a rising interest in the development of nature-based composites as recyclable, biodegradable and renewable materials [15,16]. Biobased matrices along with eco-friendly natural fibers such as wood, bamboo, flax, and jute, offer promising sustainable options for developing biocomposites [17,18].

* Corresponding author at: Department of Bioresource Engineering, McGill University, Island of Montreal, QC H9X 3V9, Canada.
E-mail address: hamid.akbarzadeh@mcgill.ca (A. Akbarzadeh).

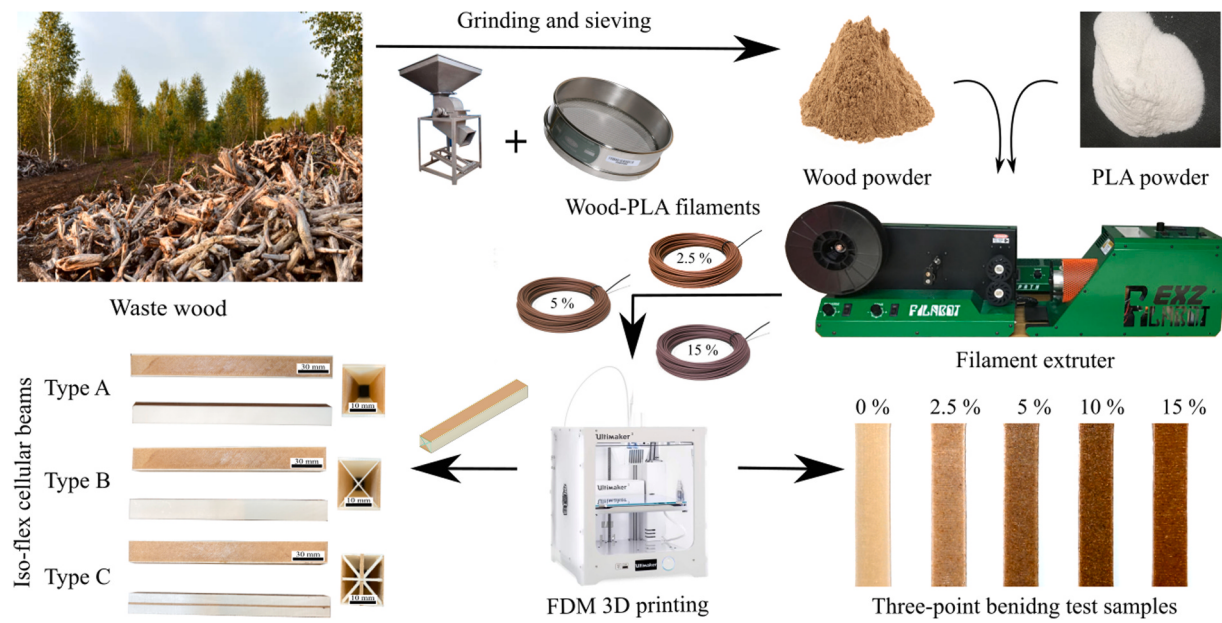


Fig. 1. Schematic view of WF-PLA filament fabrication process and 3D printed solid and cellular specimens for three-point bending tests.

A recent investigation on WF-PLA composites, achieved through blending inexpensive waste wood fiber with PLA, highlights pathways for creating sophisticated sustainable materials with intricate architecture and controlled wood-fiber contents [11]. The addition of readily available waste wood fibers leads to lower material manufacturing costs and improved thermomechanical properties (such as modulus of elasticity, ultimate strength, and thermal conductivity) of the plain polymer [11,19]. Utilizing wood waste for biopolymer composites extends their application beyond conventional inefficient combustion process [20]. The forestry and agricultural wastes can be combined with biopolymers to transform into sustainable 3D printing filaments for alternative material extrusion methods as an alternative to traditional composite manufacturing methods using injection molding and hot pressing [21]. Fused Deposition Modeling (FDM), a prominent 3D printing technique, is cost-effective, adaptable to various materials, and suited for multi-material printing [22]. Recent research on 3D printed WF-PLA composites has concluded that the type and weight proportion of wood fibers in the filaments substantially impact the performance of the 3D printed composites [23]. WF-PLA composites with specific wood fiber amounts counteract PLA's brittleness and low strength while lowering production costs, enhancing sustainability and load-bearing capacity in 3D printed materials [11].

Producing architected cellular composite structures with controllable flexural properties using biobased material resources (i.e., PLA biopolymer) and cellulose-based wastes (i.e., wood fibers) can be a critical step in the development of sustainable design and manufacturing of high-performance materials for applications in construction, automotive, aerospace, and even sports goods. Despite some research in this area [24], the effects of wood fiber proportions on flexural properties of 3D printed WF-PLA composites remain understudied. Furthermore, to the best of the authors' knowledge, no research has been conducted on the application of waste wood fiber on the rational design of 3D printed WF-PLA composite structures, such as beams and plates, with desired flexural properties, while recent advances in the additive manufacturing technology have highlighted the potential of fabricating lightweight fiber-reinforced cellular composite structures with enhanced mechanical properties [25–27].

This study aims to introduce a methodology to design and 3D print sustainable, cost-effective, load-bearing architected natural-based composite beams. This is achieved *first* by investigating the effect of adding wood fibers on the flexural properties (i.e., flexural stiffness,

rigidity, strength and failure strain) of 3D printed composite samples with a PLA biopolymeric matrix, and *second* by developing novel multi-material quasi-isotropic cellular hollow beams with engineered cell topology and rational material composition distribution (i.e., different wood fiber-to-PLA weight percentage for different members of the cellular cross section) to surpass the flexural properties of the single material cellular beam counterpart and exhibit a quasi-isotropic flexural stiffness. **Section 2** presents the manufacturing process for wood-fiber reinforced polylactic acid (WF-PLA) composite filaments, in which PLA powder is mixed with wood fibers in alternative weight percentages (2.5%, 5%, 10%, and 15%) and extruded through a single filament extruder to make biocomposite filaments that are fed into a double extruder material extrusion 3D printer to fabricate test samples. **Section 3** analyzes the flexural mechanical properties of 3D printed sustainable composite samples using three-point bending tests to compare their performance with pure PLA samples and to describe a systematic approach for designing multi-material cellular beams, based on a 2D cellular cross-section with one or two reflection symmetries, with isotropic bending behavior. Finally, the designed multi-material cells are 3D printed to be examined under a three-point bending test experiment. Detailed finite element modeling (FEM) is also performed to supplement the experimental results on these quasi-isotropic cellular solids.

This study advances and promotes additive manufacturing through the exploration of producing multimaterial structures, emphasizing the exceptional properties achievable via multimaterial design—an achievement beyond the reach of conventional manufacturing. The novel method introduced for producing hardwood fiber-PLA filaments innovatively addresses additive manufacturing's material aspect. The investigation delves into material extrusion printing using these fiber-reinforced filaments, culminating in tangible property enhancements. This transformative shift, underpinned by sustainable biomaterial integration and additive manufacturing principles, is poised to reshape high-performance materials and structural design, ushering in a new era of engineering and manufacturing potential. The research's findings showcase increased flexural properties through optimal wood fiber incorporation—enhanced modulus, rigidity, strength, and failure strain—simultaneously reducing material density and enabling lightweight, improved materials. Engineered cellular beams with varied wood-to-PLA ratios exhibit enhanced bending rigidity and quasi-isotropic flexural properties. This study exemplifies the development

Table 1

3D printing process parameters for material extrusion.

Filament type	Printing temperature [°C]	material extrusion 3D printing parameter	Value
Commercial white PLA	210	Layer height [mm]	0.2
Pure PLA	190	Bed temperature [°C]	70
2.5% WF-PLA	190	Maximum print speed [mm/min]	35
5% WF-PLA	185	Nozzle diameter [mm]	0.8
10% WF-PLA	180	Filament diameter [mm]	2.8 ± 0.1
15% WF-PLA	180	Infill [%]	100

potential for high-performance, sustainable, and cost-effective advanced materials through meticulous microarchitectural design, aligning with the essence of additive manufacturing promotion.

2. Experimental Section

2.1. Material specification and processing of WF-PLA composite filament

The WF-PLA composite filaments are made using pulverized PLA-4043D (supplied by FILABOT, Barre VT, USA; detailed specifications are provided in Table S1, Supporting Information) and wood fibers extracted from a recycled woodblock (more information about the supplier and fiber shape characteristics are given in Section S1, Supporting Information). It is important to note that our WF-PLA composites, including both filament and architected cellular structures, are compared to those made out of pure PLA-4043D and a commercial white PLA filament (supplied by Shop3D.Ca; detailed specifications on white PLA filament are given in Table S1 in Supporting Information). A single screw extruder Filabot EX2 (FILABOT, Barre VT, USA, detailed specifications are given in Table S2, Supporting Information) is utilized in this research to produce WF-PLA composite filaments with different weight percentages (2.5, 5, 10, and 15 wt%) where the wood-fiber weight percentage is calculated by:

$$wt\% = \frac{M_w}{M_w + M_{PLA}} \quad (1)$$

where M_w and M_{PLA} are the wood fiber and PLA weight, respectively. In the initial step, a blend of PLA powder and untreated sieved wood fibers with no chemical additive is prepared. This mixture is then dried in an oven at 80 °C for half an hour before being fed into the Filabot extruder for filament production, utilizing a nozzle with a diameter of 3 mm and maintaining an extrusion temperature of 185 ± 3 °C. By adjusting the feed screw driver speed 17 ± 2 rpm and spooler pulling speed 28 ± 1 mm/s, an average filament diameter of 2.8 ± 0.1 mm is achieved, ensuring optimal compatibility with the Ultimaker S3 double extruder material extrusion printer (Ultimaker B.V, Massachusetts 01701, USA, detailed specifications are given in Table S2, Supporting Information). The fabrication process is schematically shown in Fig. 1.

2.2. 3D printing and testing setup of WF-PLA composite samples

The 3D models are generated using SolidWorks and then imported into Ultimaker Cura (version 5.2.2) to be 3D printed by Ultimaker S3. Different parameters for 3D printing, such as extruding and bed temperatures, layer thickness, printing speed, and nozzle diameter, are adjusted to achieve the best quality for the printed parts. The specific settings used for the final prints can be found in Table 1 for reference. Different temperatures are utilized during filament extrusion to accommodate the viscosity differences between wood and molten PLA composite at varying wood percentage compositions. As the wood percentage increases, the PLA content per filament length decreases, necessitating less heat flow for melting. Additionally, the higher thermal conductivity of wood fiber relative to PLA [11,28] requires a reduced temperature gradient for the same heat flow rate, resulting in a lower

chosen printing temperature. This selection results in a temperature decrease of less than 6%, thus maintaining controlled conditions. While the impact of manufacturing parameters on the structural behavior of 3D printed parts has been established in previous studies [29,30], the primary emphasis of this paper lies in examining the influence of material composition and cell topology on the structural properties of 3D printed composite parts. Therefore, all manufacturing parameters are kept identical for the 3D printing of all specimens.

According to the ASTM D790 standard [31], a minimum of five cuboid samples (measuring 3.2 × 12.7 × 64 mm³) are 3D printed for each type of filament considered, including pure PLA, WF-PLA with 2.5, 5, 10, and 15 wt%, as well as commercial white PLA for comparison purposes. The 3D printed samples utilize a linear infill pattern (0/ ± 45/90 quasi-isotropic in-plane orientation), as illustrated in Fig. 1. Three-point bending tests are performed using an ADMET mechanical test machine equipped with an MTESTQuattro (ADMET, Norwood, MA, USA) testing control system and a 20 KN load cell. Before testing, the samples are stored in a laboratory atmosphere condition (23 °C and 50% relative humidity) for 40 h, and the tests are conducted at a 3 N preload and a 5 mm/min test speed condition.

The flexural stress (σ_f), strain at outer surfaces (ϵ_f), flexural modulus (E_f) and flexural rigidity (EI_f) of the samples are calculated using the extracted force-displacement curves and the following equations for a simply supported beam with a rectangular ($b \times d$) cross-section [32]:

$$\text{Flexural stress at outer surface (MPa)} \quad \sigma_f = \frac{3Fl}{2bd^2} \quad (2a)$$

$$\text{Flexural strain at outer surface (mm/mm)} \quad \epsilon_f = \frac{6\delta d}{l^2} \quad (2b)$$

$$\text{Flexural modulus (MPa)} \quad E_f = \frac{\sigma_f}{\epsilon_f} = \frac{l^3}{4bd^3} m \quad (2c)$$

$$\text{Flexural rigidity (N.mm}^2\text{)} \quad (EI)_f = \frac{l^3}{48} m \quad (2d)$$

where F and δ are the transverse load (N) and deflection (mm) at the middle of the 3D printed beam, $m = \frac{F}{\delta}$ is the slope of the initial linear elastic portion of the load-deflection curve (N/mm) and l , b and d are the beams' support span, width, and depth/thickness (mm), respectively. The flexural strength and failure strain of the outer surface can be determined by substituting the maximum force (F_{max}) and the corresponding deflection (δ_{max}) into Eqs. (2a) and (2b), respectively. The provided Eqs. (2a) to (2c) are specifically applicable to solid beams whereas Eq. (2d) can also be used for the cellular beams.

2.3. Engineered cellular WF-PLA composites

In the preceding sections, a practical and cost-effective methodology for manufacturing the sustainable 3D printed PLA products with enhanced flexural properties by utilizing WF-PLA filaments. Inspired by cellular-based *mechanical metamaterials* with anomalous properties (e.g., negative incremental stiffness [33], negative Poisson's ratio [34], and ultrahigh multifunctional figures of merits [35–39]), the topology of

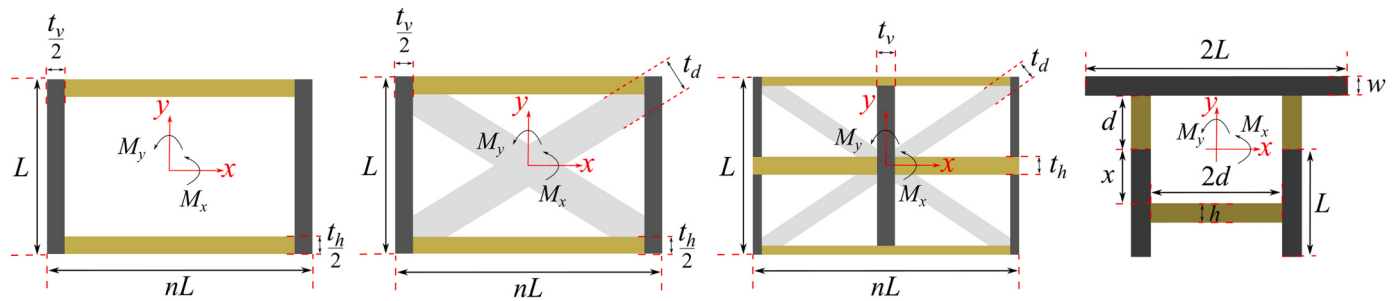


Fig. 2. Non-square *Isoflex* composite cells with width-to-height ratio (n) equal to 1.5 (different colors represent distinctive materials (Type A to D)).

underlying architecture and the material composition of wood-fiber reinforced composites can be engineered to further tune and enhance the flexural properties (with respect to weight) of WF-PLA composite beams.

To achieve an efficient and multifunctional engineered cellular materials/structures, it is critical to optimize and potentially differentiate the rigidity of struts forming the cell architecture. While altering the rigidity of a strut can be accomplished by adjusting factors such as the material and thickness, the ability to control rigidity by customizing fiber characteristics, such as fiber volume fraction and fiber orientation, provides improved adhesion between cell parts/layers constructed from the same matrix but with differing fiber characteristics, ultimately resulting in superior overall mechanical properties and manufacturability [40]. Furthermore, this approach presents a strategy to enhance the effective flexural rigidity of the cellular beam without simultaneously increasing the relative density of the cell or the weight of the structure. Following these advantages, multi-material hollow beams with 2D cellular architectures, as their cross-section, with one or two reflection symmetries are designed to achieve isotropic flexural rigidity in cellular composite beams, whereby the desired specific rigidity of the cell's struts is achieved by adjusting the fiber content and thickness. Given that cellular architectures often feature intricate geometries that cannot be produced using conventional manufacturing methods, material extrusion using fiber-reinforced materials imparts a feasible approach for fabricating complex architectures for developing sustainable and programmable structural elements.

This paper introduces an analytical methodology to design novel multi-material cellular architectures with isotropic bending rigidity (termed "*Isoflex*") through the engineering of constituent cell topology and members' material composition. Fig. 2 shows the following four types of multi-material *Isoflex* cells investigated here:

Type A: *Isoflex* rectangular composite cell made out of two materials.

Type B: *Isoflex* rectangular composite cell with diagonal bracings made out of three materials.

Type C: *Isoflex* rectangular composite cell with horizontal, vertical and diagonal bracings made out of three materials.

Type D: *Isoflex* composite cell with one reflection symmetry made out of two material compositions.

The isotropic bending conditions for cellular hollow beams are derived by equalizing the flexural rigidity of the idealized *Isoflex* cells in the x and y -directions and by solving for the members' thicknesses and modules of elasticity. Following a concise overview of the implemented methodology, the subsequent sections focus on the additive manufacturing of *Isoflex* cellular composite structures using WF-PLA. Numerical investigations and a series of experimental tests are performed to examine the impact of the rationally designed cell micro-architecture and material composition on controlling the bending performance of cellular composite beams.

Considering the anisotropic bending behavior of non-square cells with one reflection symmetry, a 2D extruded cellular architecture with an isotropic flexural rigidity is designed using the same strategy. The idea is developed by tuning the wall thickness and the material (wood

fiber content percentage) of the struts forming the cellular cross-section of hollow beams and introducing additional horizontal (h), vertical (v), and diagonal (d) bracing members to minimize the directional nature of flexural rigidity properties of the cell (mathematically expressed by $I_{xx} = I_{yy}$ and $I_{xy} = 0$). The conditions for the designed multi-material cellular architecture to have isotropic flexural rigidity are given in Table 2.

Using the cell's flexural rigidity (EI) about the x - and y -axis, the flexural rigidity isotropy of the *Isoflex* cellular beam is assessed by calculating the flexural rigidity ratio ($\alpha = EI_{yy}/EI_{xx}$), with a value of unity indicating a beam with isotropic flexural rigidity. Three distinct combinations of elasticity modulus and thickness are taken into account for the horizontal, vertical, and diagonal members (Fig. 2). It is worth mentioning that due to the inherent symmetry of the selected cell architecture, $I_{xy} = 0$, and hence if $I_{xx} = I_{yy}$ the cell shows the same flexural rigidity equal to $\frac{EI_{xx}+EI_{yy}}{2} = EI_{xx} = EI_{yy}$ in all arbitrary directions θ based on the Mohr circle [32]:

$$I_{\theta\theta} = \frac{I_{xx} + I_{yy}}{2} + \frac{I_{xx} - I_{yy}}{2} \cos 2\theta - I_{xy} \sin 2\theta \quad (3)$$

The slender members within the cell can be constructed using anisotropic materials. As the mechanical behavior of these two-force members primarily relies on the effective Young's moduli of their constituent solids along their length, without losing generality and accuracy, hypothetical isotropic mechanical behaviors (equivalent to the longitudinal mechanical properties of the members) are assumed instead of anisotropic properties. Furthermore, the effect of Poisson's ratio can be neglected in a two-force member when the member is slender, and its cross-sectional dimensions are relatively small compared to its length [32].

The equations given in Table 2 can be extended for cellular beams containing more than one cell in their cross sections. The cross-section of the chosen multi-cell beam exhibits intrinsic symmetry, leading to a moment of inertia value of zero in the xy -plane ($I_{xy} = 0$). The criterion for achieving isotropic rigidity in a beam featuring $k_x \times k_y$ *Isoflex* cells in its cross-section involves equating EI_{xx} and EI_{yy} as outlined below:

$$EI_{xx} = k_x [k_y (EI_{xx}^0) + L^2 AS_x] \quad (4a)$$

$$EI_{yy} = k_y [k_x (EI_{yy}^0) + n^2 L^2 AS_y] \quad (4b)$$

$$k_x [k_y (EI_{xx}^0) + L^2 AS_x] - k_y [k_x (EI_{yy}^0) + n^2 L^2 AS_y] = 0 \quad (4c)$$

where (EI^0) is the flexural rigidity for a single cell (given in Table 2); S_x , S_y and A can be determined as presented in Table 3.

Section 3.3.1 verifies predictions of the analytical equations for multiple *Isoflex* composite cells with detailed numerical analysis and experimental tests.

To show the methodology's versatility, a bimaterial 2D cellular architecture with only one reflection symmetry (Type D) is chosen to show isotropic flexural rigidity properties by adjusting the members'

Table 2Calculating the flexural rigidity of a cellular hollow beam made of an *Isoflex* cell.

Flexural Rigidity	Cell Type A
EI_{xx}	$\frac{(EI_{xx})_h}{E_h} \frac{t_h \left(\frac{1}{3} t_h^2 + (L + L_1)^2 \right) L_2}{16}$
EI_{yy}	$(EI_{xx})_v \frac{n_{vh} E_h t_v L^3}{12}$ $(EI_{yy})_h \frac{E_h t_h (L_2)^3}{12}$ $(EI_{yy})_v \frac{L t_v \left(\frac{1}{3} t_v^2 + (nL + L_2)^2 \right)}{n_{vh} E_h 16}$
EI_{xx}	$EI_{xx} = (EI_{xx})_h + (EI_{xx})_v \text{ and } EI_{yy} = (EI_{yy})_h + (EI_{yy})_v$ If $EI_{xx} = EI_{yy}$ then $(I_{xx})_h + n_{vh}(I_{xx})_v - (I_{yy})_h - n_{vh}(I_{yy})_v = 0$
EI_{yy}	Flexural Rigidity
EI_{xx}	$(EI_{xx})_h \frac{E_h t_h L_2 \left(\frac{t_h}{3} + (L + L_1)^2 \right)}{16}$ $(EI_{xx})_v \frac{n_{vh} E_h L^3 t_v}{12}$ $(EI_{xx})_d \frac{n_{dh} E_h}{18 L_1 (L_2)^4} \{ 1.5(L_1)^4 (L_2)^5 - 0.25(t_d \sqrt{(L_1)^2 + (L_2)^2} - L_1 L_2)^3 - (t_d L_2 \sqrt{(L_1)^2 + (L_2)^2} - L_1 - (L_2)^2) - 0.25(t_d \sqrt{(L_1)^2 + (L_2)^2} - L_1 L_2)(t_d L_2 \sqrt{(L_1)^2 + (L_2)^2} - L_1 - (L_2)^2)((t_d \sqrt{(L_1)^2 + (L_2)^2} - L_1 L_2)^2 + (t_d \sqrt{(L_1)^2 + (L_2)^2} + 2L_1 L_2)^2) \}$
EI_{yy}	$(EI_{yy})_h \frac{E_h t_h (L_2)^3}{12}$ $(EI_{yy})_v \frac{n_{vh} E_h L_v t_v^2}{16} + \frac{(nL + L_2)^2}{16}$ $(EI_{yy})_d \frac{n_{dh} E_h}{18 (L_1)^3 (L_2)^4} \{ 1.5(L_1)^4 (L_2)^7 - 0.25(t_d \sqrt{(L_1)^2 + (L_2)^2} - L_1 L_2)((L_2)^2 (t_d \sqrt{(L_1)^2 + (L_2)^2} + 2L_1 L_2)^2 + (t_d L_2 \sqrt{(L_1)^2 + (L_2)^2} - L_1 (L_2)^2)^2)(t_d L_2 \sqrt{(L_1)^2 + (L_2)^2} - L_1 (L_2)^2) - 0.25(t_d \sqrt{(L_1)^2 + (L_2)^2} - L_1 L_2)^3 \}$
EI_{xx}	Flexural Rigidity
EI_{yy}	Cell Type C
EI_{xx}	$(EI_{xx})_h \frac{E_h t_h \left(\frac{5}{3} t_h^2 + (L + L_1)^2 \right) L_2}{16}$ $(EI_{xx})_v \frac{n_{vh} E_h t_v (L_1) \left(\frac{5}{3} (L_1)^2 + (L + t_h)^2 \right)}{16}$ $(EI_{xx})_d \frac{n_{dh} E_h}{144 n^3} \frac{-(n^2 + 1)^2}{\left(-n^3 (L_1 - t_h) \frac{9L^2 (L_2 - t_v) + (L_1 - t_h)^2 (3nL - 6t_v)}{3} + 2 \left(\left(t_d + \frac{t_v}{\sqrt{n^2 + 1}} + 2n \frac{L_1}{\sqrt{n^2 + 1}} \right)^2 + (n^2 + 1)^2 \right) \right)} \left(t_d + t_v \frac{1}{\sqrt{n^2 + 1}} - n \frac{L + 2t_h}{\sqrt{n^2 + 1}} \right)^2 \left(t_d + \frac{t_v}{\sqrt{n^2 + 1}} - \frac{nL_1}{\sqrt{n^2 + 1}} \right) \left(-nL_1 + t_d \sqrt{n^2 + 1} + t_v \right) + 2 \left(t_d + \frac{t_v}{\sqrt{n^2 + 1}} - \frac{nL_1}{\sqrt{n^2 + 1}} \right)^3 \left(-nL_1 + t_d \sqrt{n^2 + 1} + t_v \right)$
EI_{yy}	$(EI_{yy})_h \frac{E_h t_h L_2 \left(\frac{5}{3} (L_2)^2 + (nL + t_v)^2 \right)}{16}$ $(EI_{yy})_v \frac{n_{vh} E_h t_v L_1 \left(\frac{5}{3} t_v^2 + (nL + L_2)^2 \right)}{16}$

(continued on next page)

Table 2 (continued)	
Flexural Rigidity	Cell Type A
	$(EI_{yy})_d = n_{dh} E_h \frac{-\sqrt{n^2+1}}{144n} \left((-n)(L_2 - t_v) \frac{9L^2 n^2 (L_1 - t_h) + (3L - 6t_h)(L_2 - t_v)^2}{\sqrt{n^2+1}} + 2(nL - nt_h - t_d \sqrt{n^2+1} + 2t_v)^2 + \frac{(2nL + nt_h + t_d \sqrt{n^2+1} - 2t_v)^2}{\sqrt{n^2+1}} \left(t_d + t_v \frac{1}{\sqrt{n^2+1}} - \frac{nL_1}{\sqrt{n^2+1}} \right) \left(-nL_1 + t_d \sqrt{n^2+1} + t_v \right) + 2(t_d + t_v \frac{1}{\sqrt{n^2+1}})^2 \right)$ $\text{If } EI_{xx} = EI_{yy} \text{ then } (L_{xx})_h + n_{vh}(L_{xx})_v + n_{dh}(L_{xx})_d - (L_{yy})_h - n_{vh}(L_{yy})_v - n_{dh}(L_{yy})_d = 0$ $* n_{vh} = E_v/E_h, n_{dh} = E_d/E_h, L_1 = L - t_h, L_2 = nL - t_v \text{ and } h, v \text{ and } d \text{ subscripts refer to horizontal, vertical, and diagonal struts of the cell, respectively.}$

thickness and the material (wood fiber content percentage). The presence of a single reflection symmetry in Type D cell architecture results in zero rigidity in the xy plane. To achieve isotropic bending rigidity, it is necessary to ensure equal flexural rigidity around both the x and y axes, which can be determined by satisfying the following condition:

$$Lw \left(d + \frac{w}{2} - \frac{L}{2} \right) + n_{12} dh \left(\frac{d}{2} - x - \frac{h}{2} \right) = 0 \quad (5)$$

where L, w, d, x and h are the dimensions shown in Fig. 2; the module of elasticity ratio of material 1–2 is presented by n_{12} .

2.4. 3D printing and testing setup of architected cellular WF-PLA composite beam

In order to evaluate the flexural rigidity of the fabricated architected cellular structures, cellular beams are 3D printed following the process outlined in Section 2.2, and subsequently subjected to three-point bending tests. In order to achieve a distinct modulus of elasticity and an optimized printability, white PLA and WF-PLA 5 wt% are selected for fabricating the bimaterial samples. Considering the constraints imposed by the printing process, such as nozzle size and the minimum cell wall thickness, WF-PLA 5 wt% is chosen to form the horizontal struts of the cellular structure. Samples made out of two materials (i.e., white PLA and WF-PLA 5 wt%) are 3D printed separately using a dual extruder Ultimaker printer and bonded using a biodegradable adhesion. Wall thicknesses of the WF-PLA horizontal members, white PLA diagonal members, and white PLA vertical members are shown in Fig. 3 as t_h , t_d and t_v , respectively. The cohesion between PLA and WF-PLA components was achieved through the application of an extremely fine layer of biodegradable bonding material (i.e., Cyanoacrylate) [41]. Benefiting from their common PLA matrix, these elements demonstrated robust adhesion, and no instances of debonding were detected throughout the three-point bending test. Furthermore, it is noteworthy that failure did not initiate at the material interface, indicating the effectiveness of the bonding approach. The restrictions of the Ultimaker material extrusion printer pose limitations on the manufacturing process for the minimum wall thickness of cell members in the beam cross-section and the maximum beam length have implications for experimental testing accuracy. In this study, a beam thickness was chosen that is one-tenth of the beam length to minimize the error in the experimental results. The specific values selected for the beam thickness and length are 19.18 mm and 191.8 mm, respectively.

Fig. 3 also presents some possible combinations of geometrical features (i.e., t_h , t_v , t_d and n) for Isoflex cells of Type A to C made of 5 wt % WF-PLA for horizontal members and white PLA for other members ($n_{vh} = n_{dh} = 0.4$) and the beam thickness of 19.18 mm. The manufacturing process for 3D printing places a constraint on the minimum value of t_h , which should be 1.6 mm due to the 0.8 mm nozzle used for printing 5 wt% WF-PLA. Additionally, the minimum values for t_v and t_d should be 0.5 mm and 0.25 mm, respectively, as the 0.25 mm nozzle is used for printing the vertical and diagonal members. To show the maximum improvement in flexural rigidity ratio to have isotropic flexural rigidity, the dimensions provided in Table 4 are selected for the test samples while considering the manufacturing limitations.

At least three replicas are 3D printed for each of the single-material and multi-material Isoflex cellular beams out of the white PLA and 5 wt% WF-PLA filaments. In all samples, except for Type A, the PLA components were printed out of plane, whereas in Type A, PLA parts were printed in-plane on the printing bed. Conversely, all the WF-PLA components were printed in-plane on the printing bed. This orientation approach eliminated the need for additional support structures during the printing process, optimizing material usage and print quality. Previous research conducted by the authors [11] demonstrated that the modulus of elasticity of PLA samples printed in-plane and out of plane

Table 3
Values of the parameters used in Eq. (4).

Parameter		Value
S_x	k_y odd	$\frac{k_y - 1}{2\sum_0^{\frac{k_y}{2}} i^2}$
	k_y even	$\frac{k_y}{2\sum_1^{\frac{k_y}{2}} (2i - 1)^2}$
S_y	k_x odd	$\frac{k_x - 1}{2\sum_0^{\frac{k_x}{2}} i^2}$
	k_x even	$\frac{k_x}{2\sum_1^{\frac{k_x}{2}} (2i - 1)^2}$
A	Type A	$E_h [L_2 t_h + n_{vh} L_{tv}]$
	Type B	$E_h \left[n_{vh} L_{tv} + L_2 t_h + n_{dh} L_2 L_1 \left[1 - \left(\frac{t_d \sqrt{\left(\frac{L_2}{L_1} \right)^2 + 1}}{L_2} - 1 \right)^2 \right] \right]$
	Type C	$E_h \left[2n(n_{vh} t_h L_1 + t_h L_2) + n_{dh}(n(L_1 - t_h)(L_2 - t_v) - (-nL_1 + t_d \sqrt{n^2 + 1} + t_v)^2) \right]$

* $n_{vh} = E_v/E_h$, $n_{dh} = E_d/E_h$, $n_{dv} = E_d/E_v$, $L_1 = L - t_h$, $L_2 = nL - t_v$ and h , v and d subscripts refer to horizontal, vertical, and diagonal struts of the cell, respectively.

exhibited a negligible maximum difference of 9%. This minor variation has no significant impact on the current study's objectives and findings. The 3D printed architected cellular beam specimens are all 191.8 mm long, which is the maximum possible printing height for Ultimaker material extrusion printer. To keep the printing and testing conditions consistent, 3D printing parameters are chosen based on Table 1, and test settings mentioned in Section 2.2 are used for the bending tests and measuring the rigidity of the cellular specimens by using the extracted force-displacement curves and Eq. (2d). Throughout the three-point bending tests, no instances of delamination between layers within the printed samples were observed. The structural integrity and interlayer adhesion of the printed specimens remained intact under loading conditions. The experimental results are compared to the detailed numerical simulations in Section 3.3.2 to evaluate the consistency.

2.5. Detailed finite element modeling of Isoflex cellular composite beams under three-point bending

In this research, a detailed numerical simulation (implemented in Abaqus ver.2019) on the as-designed cellular structure model is conducted to examine the discussed analytical findings and experimental results. Four types of the Isoflex cellular composite beams are modeled in SolidWorks, while the dimensions and materials of the modeling are chosen based on Table 2. In order to validate the numerical analysis with experimental results, the mechanical properties of the base materials are imported into Abaqus from the outcomes of tensile tests conducted on the 3D printed dogbone samples. (Fig. S2, Section S.3, Supporting Information).

To investigate the mechanical behavior of a solid structure under static loading conditions, an 8-node linear brick element (C3D8R) type was selected as the basis for the numerical model. The mesh size was chosen to ensure sufficient spatial resolution, with a minimum of two mesh elements spanning the structure's thickness. Simulations of three-point bending tests, with loading applied along the Y-axis, are conducted using a stress analysis tool known as Finite Element Analysis (FEA). Initially, loads and constraints are assigned to the bottom and top of the

cellular samples to replicate the actual three-point bending test conditions. The supports at the bottom of the sample are assumed to be fixed, and a displacement load is applied to the middle of the sample's top surface at a rate of 5 mm/min. The reaction force in the Y direction of the beams is then determined, and the bending rigidity of the samples is calculated using the force-displacement curve and Eq. (2d). Since the primary objective is to obtain only the bending rigidity, the simulation does not consider significant deformations, and only the linear elastic response is analyzed.

3. Result and discussion

3.1. Flexural properties of WF-PLA composite

The density and three-point bending experimental data for flexural stiffness, strength, failure strain, and rigidity of all the 3D printed samples (including 6 types with a minimum of 3 replicas each) are presented in Table 5 and Fig. 4. The force-displacement curves of the samples can be found in Section S.4 of the Supporting Information. An approximate calculation is performed to evaluate the volume of voids within the samples, as described in Section S5. As shown in Fig. S4, the air occupies less than 2% of the total sample volume, indicating that the primary factor contributing to density reduction is the lower wood density compared to PLA, rather than voids within the WF-PLA composite.

According to the experimental findings, the flexural modulus and rigidity of WF-PLA increase with an increase in wood fiber content. Specifically, the flexural modulus and rigidity of 15 wt% WF-PLA are 60% and 72% higher, respectively, compared to pure PLA. However, it is observed that the flexural modulus of 15 wt% WF-PLA is only 5% higher than that of 10 wt% WF-PLA. This suggests that the flexural modulus of the WF-PLA composite does not significantly change beyond a wood fiber content of 10 wt% within the range investigated in this study (Fig. 4a, b). This is believed to occur due to inadequate dispersion of wood fibers in the samples with higher wood-fiber contents, resulting in agglomeration. This agglomeration significantly reduces the reduction of

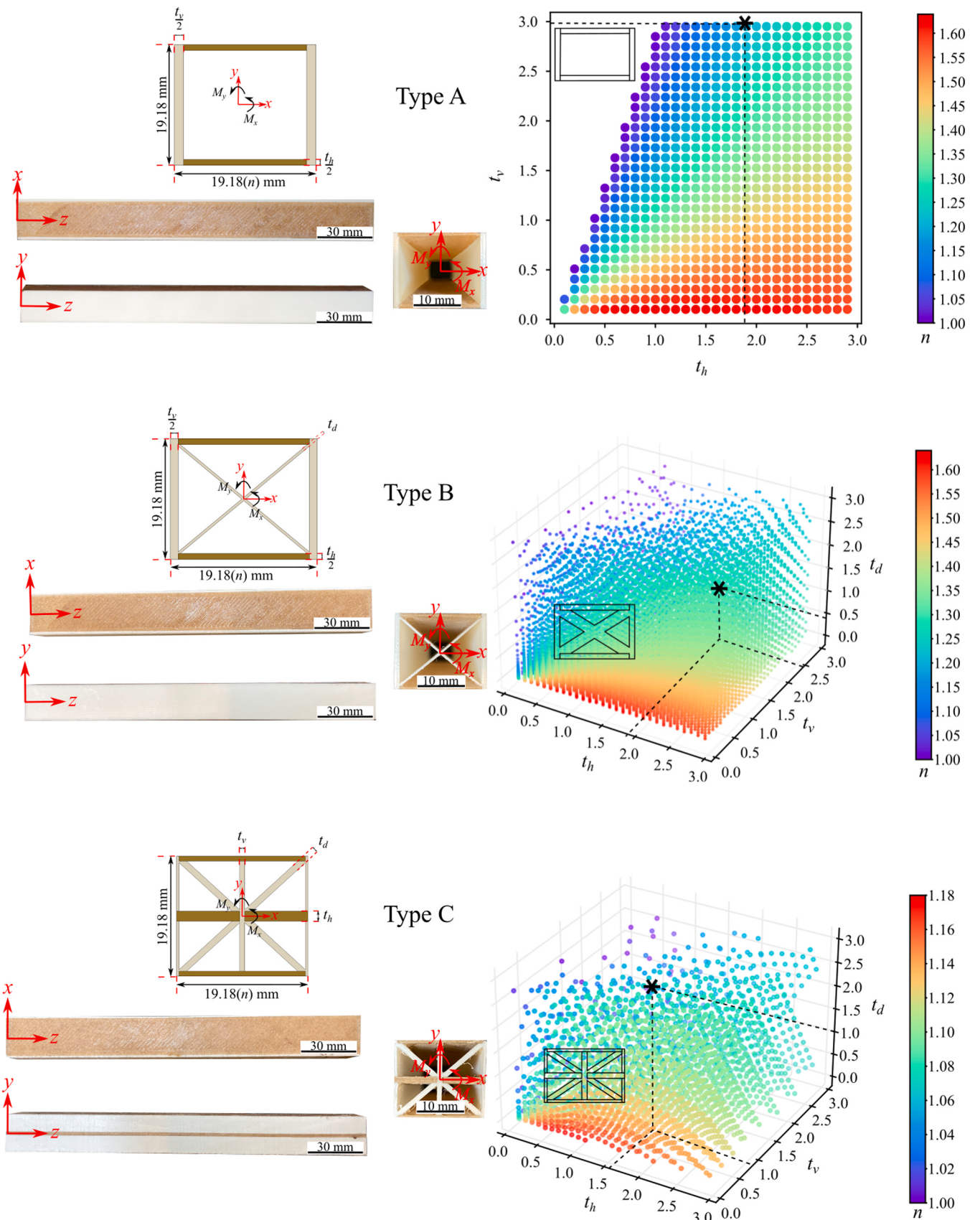


Fig. 3. Correlation between the design parameters and 3D printed WF-PLA Isoflex cellular beams (Type A, B and C) made out of white PLA and 5 wt% WF-PLA filaments. The symbol * in the figures represents the geometrical specifications of the designs used for 3D printing and conducting experiments. The values for $n_{vh} = E_v/E_h$, $n_{dh} = E_d/E_h$, t_h , t_d , t_v and n are given in Table 4.

Table 4

Geometrical and material composition parameters for *Isoflex* experiment specimen.

Cell type	<i>L</i> (mm)	<i>n</i>	<i>t_h</i> (mm)	<i>t_v</i> (mm)	<i>t_d</i> (mm)	<i>n_{vh}</i>	<i>n_{dh}</i>
Type A	19.18	1.18	1.86	2.99	-	0.4	-
Type B	19.18	1.22	1.9	2.49	0.4	0.4	0.4
Type C	19.18	1.10	1.6	0.8	1.0	0.4	0.4

**n_{vh}* = *E_v*/*E_h* and *n_{dh}* = *E_d*/*E_h*

composite stiffness [42,43]. The findings from Fig. 4c indicate that the flexural strength of the WF-PLA composite surpasses that of pure PLA when the wood fiber content is around 5 wt%. Beyond this optimal value, increasing the wood fiber content leads to a decrease in flexural strength. This decrease is likely due to the separation of wood fibers from the PLA matrix at stresses exceeding the elastic limit. In this study, no plasticizer was used for the cost-effective production of composite filaments, resulting in insufficient bonding between the wood fibers and PLA. This insufficient bonding creates gaps at the interface of the matrix and wood fibers, contributing to the diminishing trend in flexural strength. Taking into account that wood fibers exhibit higher strength than PLA [44,45], it can be observed that up to a wood fiber content of approximately 5 wt%, the addition of wood fibers enhances the flexural strength of PLA. This improvement outweighs the weakening effect caused by imperfections. However, as wood fiber content continues to increase, the presence of imperfect bonds and agglomeration becomes more significant, surpassing the strengthening effect of the fibers. When the fiber content is about 5 wt% (Fig. 4d), the flexural failure strain at the outer surface of the samples is also increased by 22% compared to the pure PLA.

In contrast to the typical *trade-offs* observed in monolithic materials [46,47] where improving one material property often leads to a decline in another property (such as trade-offs between material density and rigidity, strength and rigidity, or rigidity and flexural failure strain), WF-PLA presents a novel approach to not only addresses these common performance trade-offs but also enables the simultaneous enhancement of strength/stiffness-to-density and rigidity/failure strain-to-density ratios (as demonstrated by the 5 wt% WF-PLA composite in Fig. 4e). This advancement allows for the production of sustainable and recyclable advanced materials. By harnessing the potential of WF-PLA composites in the creation of architectural materials, an innovative category of advanced materials known as *biocomposite metamaterials* can be achieved. These materials can exhibit exceptional multifunctional properties, including ultrahigh stiffness [48], programmable stiffness [48], and geometrical reconfiguration [49]. These extraordinary characteristics arise from the combined influence of their architectural design and the composition of their constituent materials.

Table 5 provides data on the density and mechanical flexural properties of the 3D printed WF-PLA composites. The results demonstrate that the methodology described in this study successfully achieves a reduction in weight while simultaneously improving flexural stiffness, strength, failure strain, and rigidity. A regression analysis was conducted to explore the relationship between the flexural properties of WF-PLA and the weight percentage of wood fiber. The flexural modulus and

rigidity exhibit a favorable alignment with linear functions ($R^2 = 0.936$ and 0.993, respectively). However, the flexural strength and failure strain do not display a linear correlation with the wood fiber weight percentage. Notably, the regression analysis revealed a robust correlation ($R^2 > 0.99$) between the weight percentage of wood fiber (wt%) and the flexural properties of WF-PLA composites, which was effectively modeled using a four-degree polynomial equation. The corresponding empirical equations based on the experimental data, relating the flexural mechanical properties to the wood-fiber weight percentage (wt%), are presented in Table 6.

3.2. Microstructure of WF-PLA samples

The cross-sectional morphology of the fractured bending samples of WF-PLA with 10 and 15 wt% wood fiber contents is examined through scanning electron microscopy (SEM). The corresponding SEM images are presented in Fig. 5. Based on the observations from these figures, it can be noted that the reinforced samples exhibit an increase in the number and size of internal voids as the wood fiber content increases. This phenomenon is likely attributed to the presence of additional vaporized moisture and trapped air during the process of mixing wood fibers with PLA to produce the filament. Furthermore, the high porosity of wood fibers [45] has the potential to introduce trapped air into the system, resulting in the formation of void regions during the extrusion process. The presence of longer wood fibers in the feedstock relative to the diameter of the nozzle can result in inconsistent material feeding during 3D printing, which can also be another reason for the existence of internal voids in the 3D printed samples. The presence of fractured fibers observed in the cross-sectional images indicates successful load transfer between the wood fibers and PLA matrix.

Furthermore, SEM images provide evidence of wood fibers that exhibit limited efficacy in reinforcement owing to their parallel orientation with respect to the section, as well as wood fibers that have been pulled out from the PLA matrix due to inadequate fiber-matrix interfacial adhesion, compounded by fiber agglomeration. To enhance the bonding between wood fiber and Polylactic acid (PLA), various approaches can be adopted. One of them is to increase the surface area of the wood fibers to provide more bonding opportunities, which can be achieved by reducing the size of the fibers or using chemical or mechanical treatments to roughen the surface. Another method is to modify the surface of the wood fibers with chemical treatments such as acetylation or silanization to introduce functional groups that can react with the PLA and improve bonding. Additionally, coupling agents, compatibilizers, and optimized processing conditions can be used to improve the adhesion between the two materials. Maleic anhydride-grafted polypropylene (MAPP) and polyethylene-graft-maleic anhydride (PE-g-MA) have been used as coupling agents and compatibilizers, respectively, to improve the bonding between wood fibers and PLA. These approaches should be tailored based on the specific application and desired properties of the final product [50,51].

Table 5

Material density and flexural properties of White PLA, pure PLA and WF-PLA composites.

	White PLA (Commercial)	PLA 100% Wood 0%	PLA 97.5% Wood 2.5%	PLA 95% Wood 5%	PLA 90% Wood 10%	PLA 85% Wood 15%
Density [$\times 10^{-3}$ Kg.m $^{-3}$]	1.240 ± 0.011	1.153 ± 0.017	1.145 ± 0.023	1.128 ± 0.017	1.112 ± 0.017	1.096 ± 0.015
Flexural modulus [GPa]	1.27 ± 0.15	2.30 ± 0.39	2.76 ± 0.45	3.04 ± 0.34	3.47 ± 0.47	3.67 ± 0.36
Flexural strength [MPa]	58.51 ± 1.62	59.52 ± 8.25	72.21 ± 10.0	82.72 ± 3.47	82.33 ± 7.37	80.14 ± 4.84
Flexural failure strain [$\times 10^2$]	4.36 ± 0.16	2.55 ± 0.24	2.69 ± 0.37	3.09 ± 0.14	2.82 ± 0.19	2.67 ± 0.16
Flexural rigidity [$\times 10^{-4}$ N.mm 2]	6.14 ± 0.11	7.25 ± 1.24	8.19 ± 1.33	9.26 ± 1.05	11.17 ± 1.52	12.49 ± 1.22

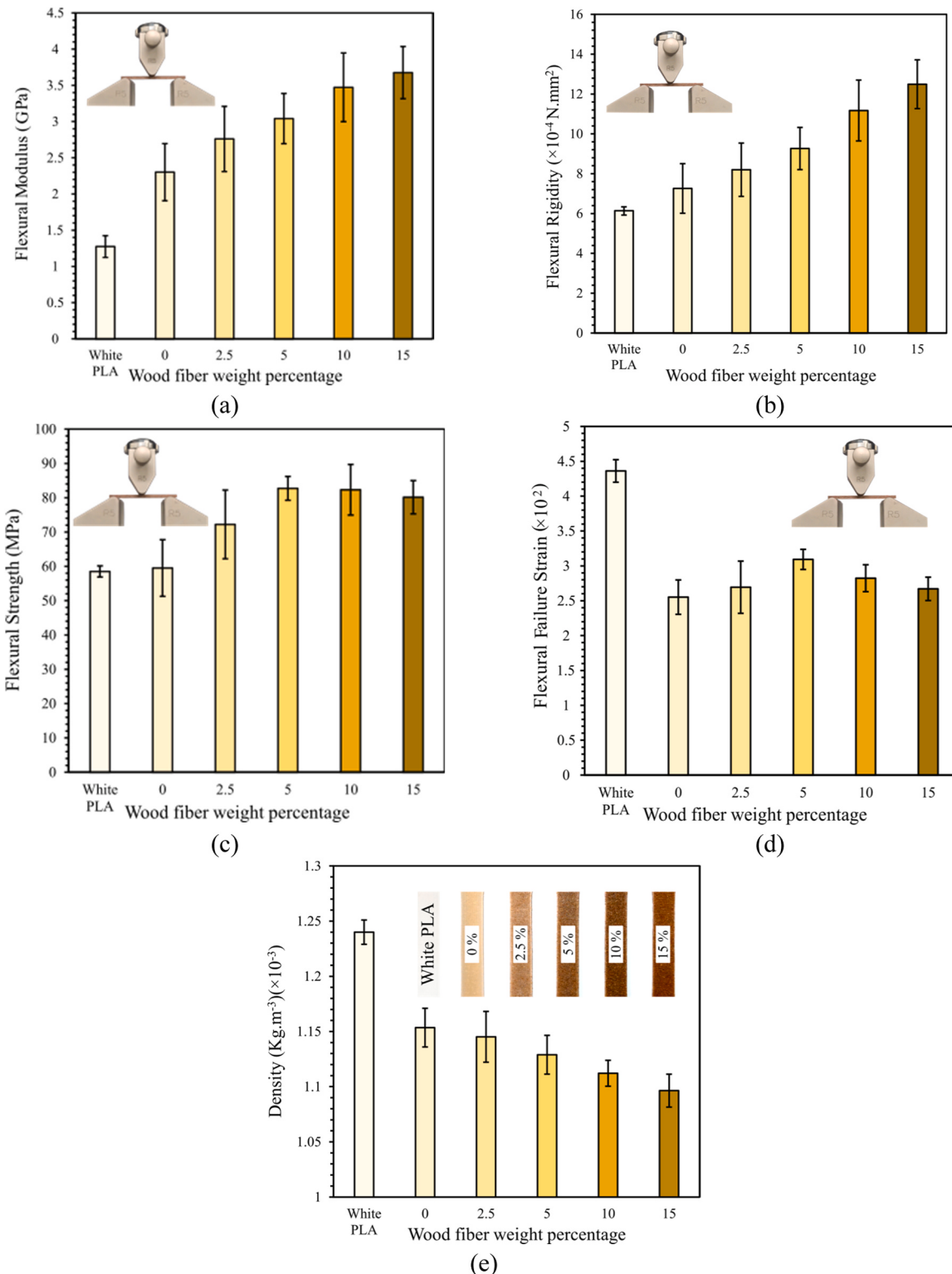


Fig. 4. Comparing flexural mechanical properties of 3D printed composites: (a) Flexural Modulus, (b) Flexural rigidity, (c) Flexural strength, (d) Flexural failure strain at outer surface and (e) Density.

Table 6

Empirical equations (regression analysis) for flexural mechanical properties of wood-fiber reinforced composite.

Property	Equation	R^2
Flexural modulus [GPa]	$E_f = -7749.967 wt^4 + 2432.327 wt^3 - 290.925 wt^2 + 24.233 wt + 2.301$	0.9998
Flexural strength [MPa]	$\sigma_f = 549009 wt^4 - 135634 wt^3 + 6018 wt^2 + 433.63 wt + 59.522$	0.9999
Flexural failure strain at the outer surface [$\times 10^2$]	$\epsilon_f = 49132 wt^4 - 13502 wt^3 + 1003.3 wt^2 - 11.723 wt + 2.552$	1.000
Flexural rigidity [$\times 10^{-4}$ N.mm ²]	$EI_f = 7513.9 wt^4 - 2906.6 wt^3 + 284.84 wt^2 + 32.2 wt + 7.2585$	0.9999

* E_f , σ_f , ϵ_f , EI_f : Flexural modulus, strength, failure strain at the outer surface and rigidity, respectively; wt.: Wood-fiber weight percentage; R^2 : Coefficient of determination.

3.3. Flexural Properties of Architected Cellular WF-PLA Composite

3.3.1. Finite element simulation

To verify the discussed analytical findings, the anisotropy of flexural rigidity of cellular beams based on the *Isoflex* architectures is numerically analyzed. Three different *Isoflex* cell types are designed based on Table 2 to evaluate and compare their isotropic bending rigidity. For all samples, the length (l) is at least 20 times greater than the cross-section width. In Fig. 6a, the analytical and simulation results for three different cell types with (i) the same height (10 cm) and width (11 cm) and (ii) the same height (10 cm) and a void fraction (0.9) (cell empty area to total cell area ratio), are compared.

Table 7 lists the cell width-to-height ratio (n), member's in-plane thicknesses, the ratio of modulus of elasticity (i.e., n_{vh} , n_{dh} , and n_{dv}) and cell relative density, which are chosen based on equations given in Table 2 in the way that it shows the maximum improvement in the flexural rigidity ratio. In order to ensure a fair comparison between our simulation results and analytical predictions, a minimum beam length-to-thickness ratio of 20 is maintained in the simulations. It should be noted that the classical Euler-Bernoulli Beam theory, which neglects the effect of transverse shear strain, tends to underestimate deflections. Nonetheless, for slender beams where the length-to-thickness ratio exceeds 20, the impact of these effects can be considered negligible [52]. The flexural rigidity ratio ($\frac{[EI]_{yy}}{[EI]_{xx}}$) of the cells based on detailed finite element analysis are compared with the samples made out of single material and provided in Fig. 6a. The isotropic rigidity properties can be seen only in *Isoflex* composite samples, which confirms the accuracy of the equations given in Table 2.

In another investigation, the cross-section is extended to more than one cell. The logarithm of the flexural rigidity ratio ($\log \frac{[EI]_{yy}}{[EI]_{xx}}$) is shown in Fig. 6b for a cross-section with k_x by k_y Cells. As shown, regardless of cell type and constituent materials, for the number of cells approximately

more than five, the most dominant parameter for the rigidity ratio is the number of cells in the x and y -directions and the cell width-to-height ratio (n). The approximate relationship is as follows:

$$\frac{[EI]_{yy}}{[EI]_{xx}} = \left(n \frac{k_x}{k_y} \right)^2, k_x \text{ and } k_y > 5 \quad (6)$$

In addition, to demonstrate the versatility of our method, an asymmetric cell is designed to exhibit isotropic bending properties by fabricating it from two materials. Fig. 6c shows the condition of two materials (elastic modulus ratio of two materials) so that the cell shows isotropic flexural rigidity. The white area in the diagram represents an area with no possible material design. As discussed in Section 3.1, choosing different fiber percentages along different cell members makes these designs possible.

3.3.2. Experimental tests

In this section, we present FEM and experimental results of three-point bending tests for WF-PLA cellular composite structures Type A, B, and C *Isoflex* cells. The aim is to further elucidate the effects of exploiting optimized material composition (a traditional approach for enhancing material properties of base materials) and architected geometry (an architected material design approach for enhancing material properties by tuning the spatial distribution of base materials). These investigations provide insights into the mechanical performance of WF-PLA composites and the role of material composition and architectural design in controlling their properties. Fig. 7a presents a comparison between the flexural rigidity ratio of *Isoflex* bimaterial samples and single material samples fabricated out of white PLA. Notably, the Experimental results reveal significant enhancements, with Type A, B and C *Isoflex* cellular WF-PLA composites incorporating 5 wt.% wood fiber exhibiting 57%, 70%, and 40% improvements in the flexural rigidity ratio to show isotropic flexural properties, respectively. Table 8 and Fig. 7b compare the specific flexural rigidity of cellular beams made

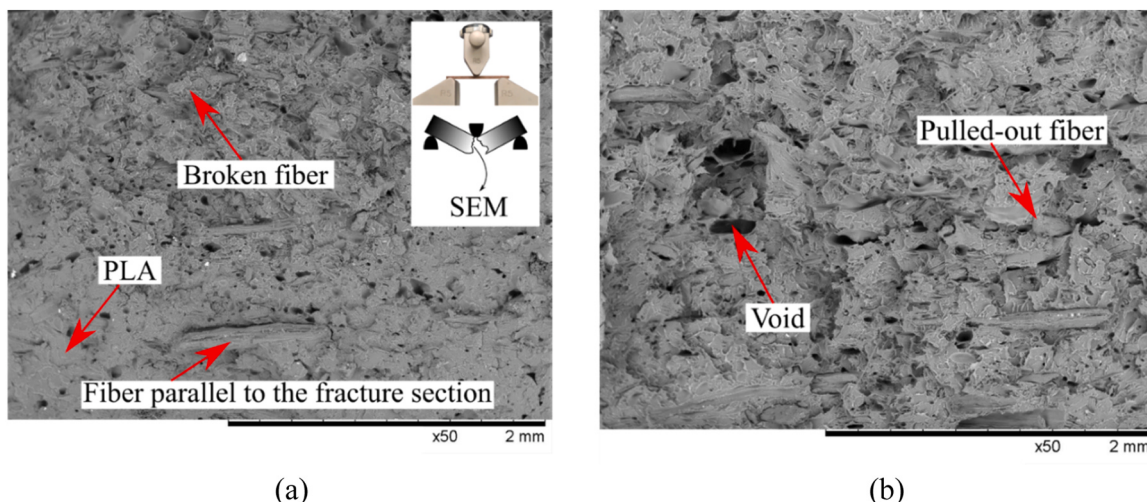


Fig. 5. SEM image of the fractured surface of 3D printed WF-PLA test samples: (a) 10 wt% and (b) 15 wt%.

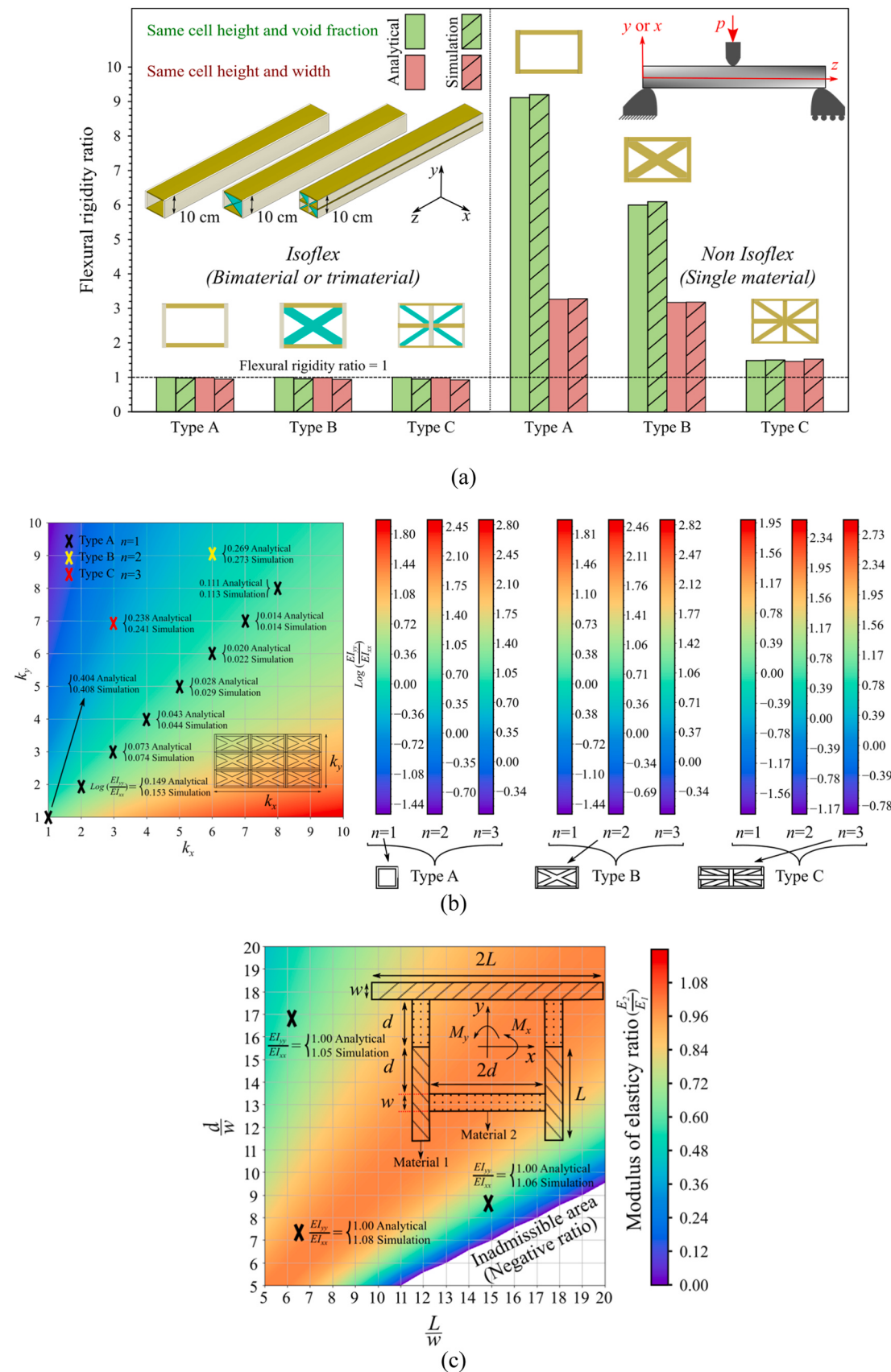


Fig. 6. Comparison of the results obtained from analytical analysis and numerical simulation: (a) the flexural rigidity ratio for different types of Isoflex cells and the samples made out of single material: (i) cells with the same height and width, (ii) cells with the same height and void fraction, (b) Log of flexural rigidity ratio for a cross-section with $k_x \times k_y$ Isoflex cells for $n = 1, 2, 3$, and (c) Ratio of the module of elasticity to have isotropic flexural rigidity for unsymmetric cell Type D.

Table 7

Geometrical and material composition parameters for Isoflex cells.

Cell type	n	t_h (mm)	t_v (mm)	t_d (mm)	n_{vh}	n_{dh}	Void fraction	
Fig. 6a	Type A	1.1	0.01	0.55	-	0.0147	-	0.95
	Type B	1.1	0.01	0.69	0.01	0.01	1.79	0.93
	Type C	1.1	0.01	0.29	0.19	0.01	0.019	0.9
	Type A	1.9	0.031	1.9	-	0.00021	-	0.9
	Type B	1.7	0.12	1.54	0.006	0.01	0.0035	0.9
	Type C	1.1	0.01	0.29	0.019	0.01	0.02	0.9

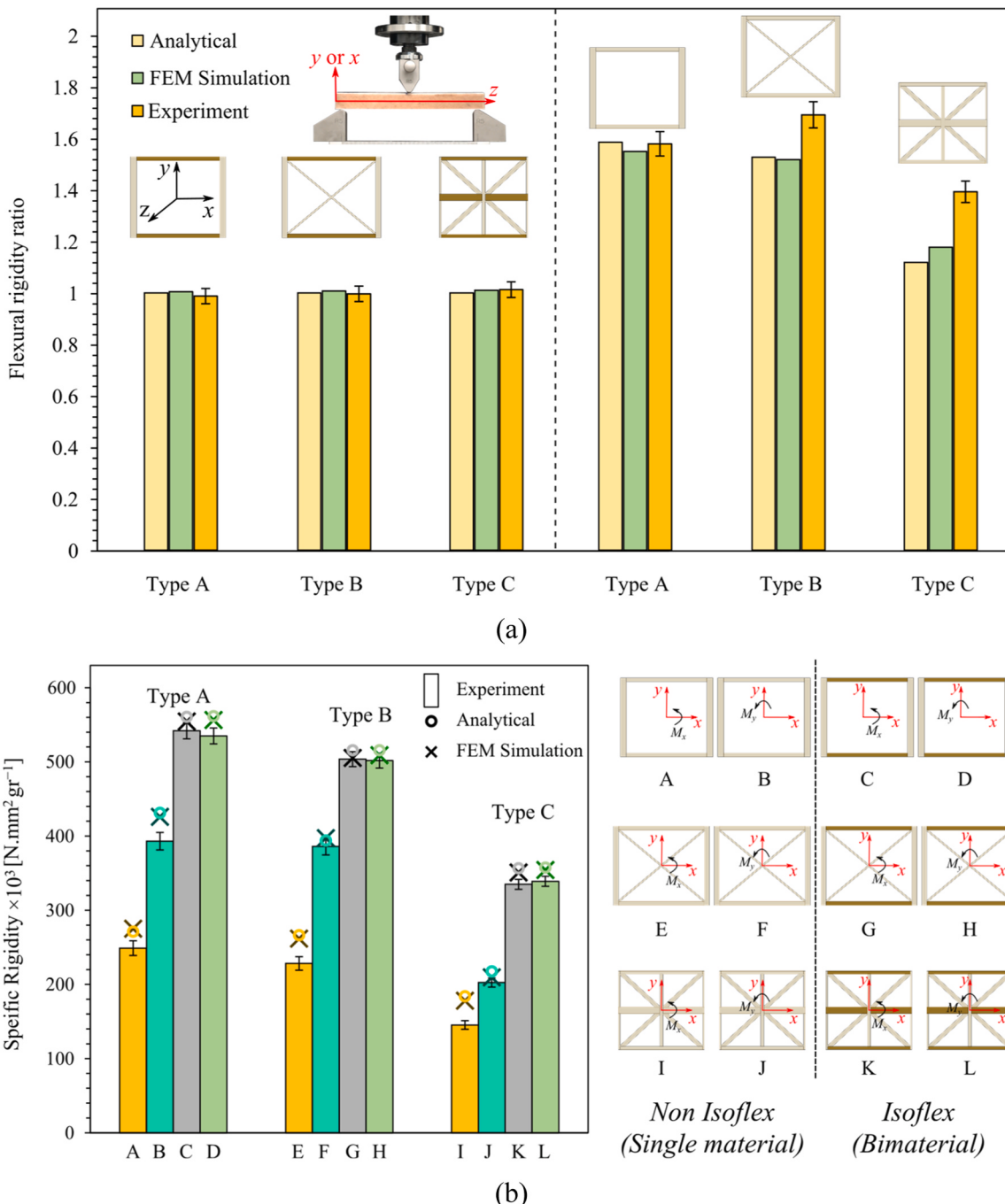
 $*n_{vh} = E_v/E_h$, $n_{dh} = E_d/E_h$.

Fig. 7. Comparison of (a) flexural rigidity ratio and (b) specific flexural rigidity (flexural rigidity over mass) obtained from the analytical modelling, experimental tests, and numerical simulation for types A, B and C of Bimaterial Isoflex cell (i.e., 5 wt% WF-PLA and white PLA) and the samples made out of one material (i.e., white PLA). Within the figure, the white material corresponds to pure white PLA, while the brown material signifies the 5 wt% WF-PLA.

Table 8

Specific flexural rigidity of White PLA and WF-PLA cellular composite structures.

		Cellular samples made out of only White PLA (Commercial) filament			Isoflex samples made out of WF-PLA filament		
Specific flexural Rigidity $\times 10^3$ [N.mm ² .gr ⁻¹]		Type A	Type B	Type C	Type A	Type B	Type C
Analytical	X direction	272.97	261.93	189.58	565.61	525.02	364.45
	Y direction	432.56	399.98	211.86	565.60	525.02	364.45
Simulation	X direction	275.01	261.68	177.89	554.33	505.16	350.62
	Y direction	425.97	397.14	209.47	556.41	508.79	354.01
Experiment	X direction	263.96 \pm 6.51	228.24 \pm 5.70	145.43 \pm 2.70	541.83 \pm 6.94	503.59 \pm 13.62	334.82 \pm 9.37
	Y direction	393.08 \pm 6.55	386.11 \pm 8.7	202.50 \pm 2.23	534.88 \pm 18.37	501.629 \pm 11.80	338.97 \pm 12.31

out of 5 wt% WF-PLA determined by conducting experimental testing (3 replicas), analytical method, and numerical simulation through detailed FEM. The results show that cellular composite structures, 3D printed out of WF-PLA filament, has higher flexural rigidity compared to the white PLA cellular specimens. For example, the test results for specific flexural rigidity (rigidity over mass) of Type A, B, and C Isoflex cellular WF-PLA composites with 5 wt% wood fiber in (x, y) directions are, respectively, (118%, 37%), (120%, 30%) and (130%, 67%) greater than their counterparts 3D printed out of pure PLA biopolymer. It is worth mentioning that during the three-point bending tests, there was no evidence of delamination between the layers upon sample failure. Examination of fracture samples in SEM image of cross-section (Fig. 5) revealed ruptured wood fibers and pulled-out fibers, indicating primary failure modes encompassing PLA matrix cracking, wood fiber fracture, and detachment at the PLA-wood fiber interface.

Taking into consideration the reduction in material density achieved through the incorporation of wood fiber into WF-PLA composites, the additive manufacturing method introduced in this study offers an opportunity to enhance the rigidity-to-weight ratio of cellular solids by utilizing an optimized material composition. Furthermore, through architectural engineering, this study introduces a distinctive strategy to tailor the flexural properties of cellular structures. The experimental findings demonstrate that 3D printed Isoflex cellular beams exhibit not only increased flexural rigidity but also isotropic flexural rigidity when compared to pure PLA 3D printed samples. The observed discrepancy between the FE analysis and experimental findings may be attributed to several factors, including inherent defects introduced during the 3D printing process and inadequate bonding between the fibers and the material, primarily caused by fiber agglomeration and the presence of voids within the manufactured samples.

4. Conclusions

This study offers an economical additive manufacturing approach for crafting advanced sustainable materials. By combining recyclable bio-based substances and 3D printing, architected wood-fiber reinforced polymeric (WF-PLA) cellular composite beams are designed and 3D printed. These sustainable composites, enabled by the capitalization of a 3D printing technology, merges wood's recyclability and biodegradability with robust flexural performance, enabling to achieve controllable structural attributes and substantial weight reduction. Mechanical assessments of 3D printed WF-PLA composites unveil heightened flexural rigidity, exemplified by a 72% increase for 15 wt% recycled wood fibers. Incorporating 5 wt% wood fibers boosts flexural strength and failure strain up to 39% and 21% at the same time. SEM micrographs of fractured surfaces validate effective load transfer between wood fibers and the PLA matrix. Leveraging rationally-designed architectures and composite solid materials, a systematic approach to designing and additively manufacturing multi-material hollow beams, termed Isoflex cellular beams, is presented. Analytical and finite element modeling outcomes, verified through three-point bending tests on 5 wt% wood fiber-containing Isoflex beams, reveal potential enhancements in the flexural rigidity ratio (up to 70% to show isotropic flexural properties) and specific flexural rigidity (up to 130%).

This study presents a novel engineering strategy where light-weighting and multifunctionality emerge from combined material and architecture engineering. This methodology facilitates the design and production of cost-effective, renewable, and biodegradable advanced structural materials, poised to revolutionize the application of eco-friendly biocomposites across aerospace, automotive, and construction sectors. Furthermore, this methodology can be extended to a variety of biocomposites made out of diverse biosourced materials, facilitated by utilizing a multimaterial additive manufacturing technology.

CRediT authorship contribution statement

Abdolhamid Akbarzadeh: Writing – review & editing, Visualization, Validation, Supervision, Resources, Project administration, Methodology, Funding acquisition, Conceptualization. **Armin Mirabolghasemi:** Writing – review & editing, Validation, Methodology, Investigation. **Larry Lessard:** Writing – review & editing, Supervision. **Ehsan Estakhrianaghghi:** Writing – review & editing, Writing – original draft, Validation, Software, Methodology, Investigation, Formal analysis, Data curation, Conceptualization.

Declaration of Competing Interest

The authors declare that they have no known competing financial interests or personal relationships that could have appeared to influence the work reported in this paper.

Data Availability

Data will be made available on request.

Acknowledgments

A.H. Akbarzadeh acknowledges the financial support by Natural Sciences and Engineering Research Council of Canada through NSERC Discovery Grant RGPIN-2022-04493, Canada Research Chairs program in Multifunctional Metamaterials, Canada Foundation for Innovation (CFI) through John R. Evans Leaders Fund, and Centre SÈVE – Centre SÈVE - sciences du végétal. A.H. Akbarzadeh and L. Lessard also acknowledge the financial support by McGill Sustainability Systems Initiative (MSSI).

Appendix A. Supporting information

Supplementary data associated with this article can be found in the online version at doi:10.1016/j.addma.2023.103800.

References

- [1] O. Al-Ketan, R. Rowshan, R.K. Abu Al-Rub, Topology-mechanical property relationship of 3D printed strut, skeletal, and sheet based periodic metallic cellular materials, *Addit. Manuf.* 19 (2018) 167–183.
- [2] Q.T. Do, C.H.P. Nguyen, Y. Choi, Homogenization-based optimum design of additively manufactured Voronoi cellular structures, *Addit. Manuf.* 45 (2021), 102057.

- [3] J.U. Surjadi, L.B. Gao, H.F. Du, X. Li, X. Xiong, N.X. Fang, Y. Lu, Mechanical metamaterials and their engineering applications, *Adv. Eng. Mater.* 21 (3) (2019), 1800864.
- [4] K. Bertoldi, V. Vitelli, J. Christensen, M. van Hecke, Flexible mechanical metamaterials, *Nat. Rev. Mater.* 2 (11) (2017), 17066.
- [5] H. Mofatteh, B. Shahryari, A. Mirabolghasemi, A. Seyedkanani, R. Shirzadkhani, G. Desharnais, A. Akbarzadeh, Programming multistable metamaterials to discover latent functionalities, *Adv. Sci.* 9 (33) (2022), 2202883.
- [6] A. Seyedkanani, A. Akbarzadeh, Magnetically assisted rotationally multistable metamaterials for tunable energy trapping–dissipation, *Adv. Funct. Mater.* 32 (52) (2022), 2207581.
- [7] A. Seyedkanani, H. Niknam, A.H. Akbarzadeh, Bending behavior of optimally graded 3D printed cellular beams, *Addit. Manuf.* 35 (2020), 101327.
- [8] J. Shi, A.H. Akbarzadeh, Architected cellular piezoelectric metamaterials: thermo-electro-mechanical properties, *Acta Mater.* 163 (2019) 91–121.
- [9] A. Mao, N. Zhao, Y. Liang, H. Bai, Mechanically efficient cellular materials inspired by cuttlebone, *Adv. Mater.* 33 (15) (2021), e2007348.
- [10] Y. Tao, W.G. Li, K. Wei, S.Y. Duan, W.B. Wen, L.M. Chen, Y.M. Pei, D.N. Fang, Mechanical properties and energy absorption of 3D printed square hierarchical honeycombs under in-plane axial compression, *Compos. Part B-Eng.* 176 (2019), 107219.
- [11] E. Estakhrianaghghi, A. Mirabolghasemi, Y.N. Zhang, L. Lessard, A. Akbarzadeh, 3D-printed wood-fiber reinforced architected cellular composites, *Adv. Eng. Mater.* 22 (11) (2020), 2000565.
- [12] C. Hu, J.Q. Dong, J.J. Luo, Q.H. Qin, G.Y. Sun, 3D printing of chiral carbon fiber reinforced polyalactic acid composites with negative Poisson's ratios, *Compos. Part B-Eng.* 201 (2020), 108400.
- [13] X. Chen, G. Chen, G. Wang, P. Zhu, C. Gao, Recent progress on 3D-printed polyalactic acid and its applications in bone repair, *Adv. Eng. Mater.* 22 (4) (2020), 1901065.
- [14] M. Heidari-Rarani, M. Rafiee-Afarani, A.M. Zahedi, Mechanical characterization of FDM 3D printing of continuous carbon fiber reinforced PLA composites, *Compos. Part B-Eng.* 175 (2019), 107147.
- [15] W. Huang, M. Shishehbor, N. Guarin-Zapata, N.D. Kirchhofer, J. Li, L. Cruz, T. Wang, S. Bhowmick, D. Stauffer, P. Manimunda, K.N. Bozhilov, R. Caldwell, P. Zavattieri, D. Kisailus, A natural impact-resistant bicontinuous composite nanoparticle coating, *Nat. Mater.* 19 (11) (2020) 1236–1243.
- [16] K. Gouda, S. Bhowmik, B. Das, A review on allotropes of carbon and natural filler-reinforced thermomechanical properties of upgraded epoxy hybrid composite, *Rev. Adv. Mater. Sci.* 60 (1) (2021) 237–275.
- [17] G. Furtos, L. Molnar, L. Silaghi-Dumitrescu, P. Pascuta, K. Kornienko, Mechanical and thermal properties of wood fiber reinforced geopolymmer composites, *J. Nat. Fibers* 19 (13) (2022) 6676–6691.
- [18] G. Furtos, L. Silaghi-Dumitrescu, P. Pascuta, C. Sarosi, K. Kornienko, Mechanical properties of wood fiber reinforced geopolymers composites with sand addition, *J. Nat. Fibers* 18 (2) (2021) 285–296.
- [19] T.Q. Tran, F.L. Ng, J.T.Y. Kai, S. Feih, M.L.S. Nai, Tensile strength enhancement of fused filament fabrication printed parts: a review of process improvement approaches and respective impact, *Addit. Manuf.* 54 (2022), 102724.
- [20] S. Sharafi, M.H. Santare, J. Gerdes, S.G. Advani, A review of factors that influence the fracture toughness of extrusion-based additively manufactured polymer and polymer composites, *Addit. Manuf.* 38 (2021), 101830.
- [21] A. Le Dugou, G. Chabaud, R. Matsuzaki, M. Castro, Tailoring the mechanical properties of 3D-printed continuous flax/PLA biocomposites by controlling the slicing parameters, *Compos. Part B: Eng.* 203 (2020), 108474.
- [22] A.N. Solodov, J. Shayimova, D. Balkaev, A.S. Nizamutdinov, K. Zimin, A. G. Kiayomov, R.R. Amirov, A.M. Dimiev, High-throughput, low-cost and “green” production method for highly stable polypropylene/perovskite composites, *Appl. 3D Print. Addit. Manuf.* 59 (2022), 103094.
- [23] A. Vedrtnam, S. Kumar, S. Chaturvedi, Experimental study on mechanical behavior, biodegradability, and resistance to natural weathering and ultraviolet radiation of wood-plastic composites, *Compos. Part B-Eng.* 176 (2019), 107282.
- [24] X. Bi, R. Huang, 3D printing of natural fiber and composites: a state-of-the-art review, *Mater. Des.* 222 (2022), 111065.
- [25] X. Gao, S.X. Qi, X. Kuang, Y.L. Su, J. Li, D.J. Wang, Fused filament fabrication of polymer materials: a review of interlayer bond, *Addit. Manuf.* 37 (2021), 101658.
- [26] Y. Xiong, Y.L. Tang, Q. Zhou, Y.S. Ma, D.W. Rosen, Intelligent additive manufacturing and design state of the art and future perspectives, *Addit. Manuf.* 59 (2022), 103139.
- [27] K. Dong, L. Liu, X. Huang, X. Xiao, 3D printing of continuous fiber reinforced diamond cellular structural composites and tensile properties, *Compos. Struct.* 250 (2020), 112610.
- [28] J. MacLean, Thermal conductivity of wood, Vol. 13, *Heating, piping & air conditioning*, Madison, USA, 1941, pp. 380–391.
- [29] G. Singh, J.M. Missiaen, D. Bouvard, J.M. Chaix, Copper extrusion 3D printing using metal injection moulding feedstock: analysis of process parameters for green density and surface roughness optimization, *Addit. Manuf.* 38 (2021), 101778.
- [30] S.M. Chang, S. Hur, J. Park, D.G. Lee, J. Shin, H.S. Kim, S. Eun, J.M. Baik, M. Kim, H.C. Song, C.Y. Kang, Optimization of piezoelectric polymer composites and 3D printing parameters for flexible tactile sensors, *Addit. Manuf.* 67 (2023), 103470.
- [31] S. ASTM, Standard test methods for flexural properties of unreinforced and reinforced plastics and electrical insulating materials. *ASTM D790*, Annu. Book ASTM Stand. (1997).
- [32] F.P. Beer, E.R. Johnston, J.T. DeWolf, D.F. Mazurek, *Statics and mechanics of materials*, McGraw-Hill Education, 2021.
- [33] J. Shi, H. Mofatteh, A. Mirabolghasemi, G. Desharnais, A. Akbarzadeh, Programmable multistable perforated shellular, *Adv. Mater.* 33 (42) (2021), e2102423.
- [34] D. Li, X. Bu, Z. Xu, Y. Luo, H. Bai, Bioinspired multifunctional cellular plastics with a negative poisson's ratio for high energy dissipation, *Adv. Mater.* 32 (33) (2020), e2001222.
- [35] X. Tian, K. Zhou, 3D printing of cellular materials for advanced electrochemical energy storage and conversion, *Nanoscale* 12 (14) (2020) 7416–7432.
- [36] X. Li, X. Yu, W. Zhai, Additively manufactured deformation-recoverable and broadband sound-absorbing microlattice inspired by the concept of traditional perforated panels, *Adv. Mater.* 33 (44) (2021), e2104552.
- [37] O. Al-Ketan, R.K. Abu Al-Rub, Multifunctional mechanical metamaterials based on triply periodic minimal surface lattices, *Adv. Eng. Mater.* 21 (10) (2019), 1900524.
- [38] Z. Jiang, J.H. Pikul, Centimetre-scale crack-free self-assembly for ultra-high tensile strength metallic nanolattices, *Nat. Mater.* 20 (11) (2021) 1512–1518.
- [39] Q.Y. Zhou, J.Y. Lyu, G. Wang, M. Robertson, Z. Qiang, B. Sun, C.H. Ye, M.F. Zhu, Mechanically strong and multifunctional hybrid hydrogels with ultrahigh electrical conductivity, *Adv. Funct. Mater.* 31 (40) (2021), 2104536.
- [40] E. Estakhrianaghghi, A. Mirabolghasemi, J. Shi, L. Lessard, A.H. Akbarzadeh, Architected cellular fiber-reinforced composite, *Compos. Part B-Eng.* 238 (2022), 109894.
- [41] S. Daane, Chapter 5 - alloplastic implantation. *Plastic Surgery Secrets Plus*, second ed., Mosby, Philadelphia, 2010, pp. 28–32. J. Weinzweig, Editor.
- [42] A.R. Ghasemi, M. Mohandes, R. Dimitri, F. Tornabene, Agglomeration effects on the vibrations of CNTs/fiber/polymer/metal hybrid laminates cylindrical shell, *Compos. Part B-Eng.* 167 (2019) 700–716.
- [43] Z. Wu, Y. Zhao, K. Yang, J. Guan, S. Wang, Y. Gu, M. Li, Y. Feng, W. Feng, R. O. Ritchie, Enhancing the mechanical performance of fiber-reinforced polymer composites using carbon nanotubes as an effective nano-phase reinforcement, *Adv. Mater. Interfaces* 10 (3) (2023), 2201935.
- [44] W.D. Liu, T.T. Chen, M.E. Fei, R.H. Qiu, D.M. Yu, T.F. Fu, J.H. Qiu, Properties of natural fiber-reinforced biobased thermoset biocomposites: effects of fiber type and resin composition, *Compos. Part B-Eng.* 171 (2019) 87–95.
- [45] T. Keplinger, F.K. Wittel, M. Rugegeberg, I. Burgert, Wood derived cellulose scaffolds-processing and mechanics, *Adv. Mater.* 33 (28) (2021), e2001375.
- [46] X. Luo, D. Li, C. Yang, A. Gebert, H. Lu, T. Song, H. Ma, L. Kang, Y. Long, Y. Li, Circumventing the strength-ductility trade-off of β -type titanium alloys by defect engineering during laser powder bed fusion, *Addit. Manuf.* 51 (2022), 102640.
- [47] Y.B. Jeong, T. Wada, S.H. Joo, J.M. Park, J. Moon, H.S. Kim, I.V. Okulov, S.H. Park, J.H. Lee, K.B. Kim, H. Kato, Beyond strength-ductility trade-off: 3D interconnected heterostructured composites by liquid metal dealloying, *Compos. Part B-Eng.* 225 (2021), 109266.
- [48] M. Peng, Z. Wen, L. Xie, J. Cheng, Z. Jia, D. Shi, H. Zeng, B. Zhao, Z. Liang, T. Li, L. Jiang, 3D printing of ultralight biomimetic hierarchical graphene materials with exceptional stiffness and resilience, *Adv. Mater.* 31 (35) (2019), e1902930.
- [49] X. Kuang, S. Wu, Q. Ze, L. Yue, Y. Jin, S.M. Montgomery, F. Yang, H.J. Qi, R. Zhao, Magnetic dynamic polymers for modular assembling and reconfigurable morphing architectures, *Adv. Mater.* 33 (30) (2021), e2102113.
- [50] R. Liu, S.P. Luo, J.Z. Cao, Y. Peng, Characterization of organo-montmorillonite (OMMT) modified wood flour and properties of its composites with poly(lactic acid), *Compos. Part a-Appl. Sci. Manuf.* 51 (2013) 33–42.
- [51] B. Effah, A. Van Reenen, M. Meimcken, Mechanical properties of wood-plastic composites made from various wood species with different compatibilisers, *Eur. J. Wood Wood Prod.* 76 (1) (2018) 57–68.
- [52] E. Witmer, Elementary bernoulli-euler beam theory, MIT, 1991, MIT Unifi--. Eng. Course Notes (1992) 114–164.